

Article

The Zinc-Air Battery Performance with Ni-Doped MnO₂ Electrodes

Anuradha Chowdhury¹, Kuan-Ching Lee², Mitchell Shyan Wei Lim² , Kuan-Lun Pan³, Jyy Ning Chen¹, Siewhui Chong² , Chao-Ming Huang^{4,*}, Guan-Ting Pan^{1,*}  and Thomas Chung-Kuang Yang^{1,*} 

- ¹ Department of Chemical Engineering and Biotechnology, National Taipei University of Technology, Taipei 106, Taiwan; anuradhachowdhary24@gmail.com (A.C.); jingsi229@gmail.com (J.N.C.)
- ² Department of Chemical and Environmental Engineering, University of Nottingham Malaysia, Selangor 43500, Malaysia; ebxk11@nottingham.edu.my (K.-C.L.); keby3mli@nottingham.edu.my (M.S.W.L.); faye.chong@nottingham.edu.my (S.C.)
- ³ Industrial Technology Research Institute, Green Energy and Environment Institute, Hsinchu 310, Taiwan; KLPan@itri.org.tw
- ⁴ Green Energy Technology Research Center and Department of Materials Engineering, Kun Shan University, Tainan 710, Taiwan
- * Correspondence: charming@mail.ksu.edu.tw (C.-M.H.); gtpan@ntut.edu.tw (G.-T.P.); ckyang@mail.ntut.edu.tw (T.C.-K.Y.)

Abstract: A rechargeable zinc-air battery shows great promise because of its high energy density, low cost, greater safety, and its environment-friendly properties. However, rechargeable zinc-air battery development has been hindered by the lack of a satisfactory bi-functional electrode. In this research, we report on a solution which uses electro-deposition to dope nickel into manganese on the stainless-steel mesh. The result shows the hydroxyl group on the prepared samples improving its oxygen reduction reaction and oxygen evolution reaction performance, as well as boosting the ion diffusion rate and stabilizing the zinc-air battery charge-discharge performance (overall potential gap dropped from 0.84 V to 0.82 V after 1000 cycles). This study contributes to our understanding of a new method for the improvement of bi-functional electrodes.

Keywords: Zinc-air battery; manganese; bi-functional electrode; Ni-doping



Citation: Chowdhury, A.; Lee, K.-C.; Wei Lim, M.S.; Pan, K.-L.; Chen, J.N.; Chong, S.; Huang, C.-M.; Pan, G.-T.; Yang, T.C.-K. The Zinc-Air Battery Performance with Ni-Doped MnO₂ Electrodes. *Processes* **2021**, *9*, 1087. <https://doi.org/10.3390/pr9071087>

Academic Editors: Adina ARVINTE and Laura Micheli

Received: 2 May 2021
Accepted: 18 June 2021
Published: 23 June 2021

Publisher's Note: MDPI stays neutral with regard to jurisdictional claims in published maps and institutional affiliations.



Copyright: © 2021 by the authors. Licensee MDPI, Basel, Switzerland. This article is an open access article distributed under the terms and conditions of the Creative Commons Attribution (CC BY) license (<https://creativecommons.org/licenses/by/4.0/>).

1. Introduction

Among a number of energy storage devices, such as electrical, mechanical, chemical, and electrochemical, the latter is the most flexible, having high energy density and scalable qualities. Hence, the essential need for an energy storage device is in high demand. Extensive research into various electrochemical energy storage devices with high efficiency and eco-friendly measures are required to solve renewable energy's intermittent and dispersal problems [1]. The successful fabrication of batteries relies on several factors, such as electrodes, appropriate electrolytes, and the rational technology for assembling it [2]. The most important factor to be kept in mind is the safety issue linked with the combustible organic electrolyte, its cost, and availability of resources. This motivates the researchers to dive deeper into the field and come up with alternative technology [3].

To support the renewable energy technologies, a number of batteries have been experimented with, and companies have come out with an impetuous excel of lithium-ion batteries as portable electronics in a commercial market. Still, with the issues of high cost, safety hazards, and constantly increasing demands of long-lasting products, the lithium-ion batteries are not successful in meeting the current energy requirements. The rapid growing market in grid-scale electricity storage devices and electric vehicles rises with the concern of raw material's availability, which is an essential component in current commercial batteries [4]. A considerable number of studies devoted to rechargeable batteries have given us the opportunity to explore a wide variety of them. The recent advancements in the

rechargeable aqueous zinc-ion battery has gained increased attention due to its large-scale grid storage capacity, environment-friendly, and strong safety features [5–7]. One of the major challenges in the development of the rechargeable zinc-air batteries are oxygen reduction reaction (ORR) and oxygen evolution reaction (OER) performance. Efforts in improving the efficiency of catalysts for ORR and OER are hindered by the unsatisfactory bi-functional oxygen catalysts or electrodes, owing to the inactive kinetics and short-lived cycles [8].

Great effort has been made to study bi-functional catalysts, which have good ORR and OER performance. ORR determines the working discharge voltage of the battery, and OER determines the charge voltage of the battery. The benchmark catalysts for ORR and OER are Pt- and Ir/Ru-based catalysts, respectively. Their application is limited by high cost, limited bi-functional activity, and weak stability. Pt coupled with different compounds, as mentioned by Meng et al. [9], showed enhanced activity along with durability for OER, ORR, as well as photocatalytic water splitting. In addition, 3.1-fold enhancement is achievable via new hybrid catalysts, comparable to the Pt/C catalyst, which opens new pathways to produce hybrid catalysts in terms of highly controllable and reproductive methods [9].

Emerging as a precious metal-based materials alternative, non-noble metal oxides are considered cost-effective ORR catalysts for zinc-air batteries. Much literature has reported on cathode materials, and among them, manganese dioxide, being the most common, exhibits diversity in crystal structure as well as multivalent states (0, +2, +3, +4, and +7). Among non-noble metal oxides, MnO_x species has been widely investigated due to its low toxicity, low cost, abundance, environmental friendliness, and excellent ORR activity properties [10]. Yet, MnO_2 suffers from disoriented features of structural transformation, low electronic conductivity, and manganese disintegration, affecting the electrochemical performance [11]. This provides us with an excellent opportunity to experiment with manganese-based batteries. However, MnO_x species, having insufficient OER active sites, hinder its usage as a bi-functional catalyst. Further, doping OER active catalysts with MnO_x species is an effective way to overcome MnO_x species catalyst defects. This is one of the effective ways to improve MnO_x species OER activity. Research shows Ni based materials are notably OER active because they have low overpotential, which make them a potential candidate for metal-based OER catalysts [10].

In this research, we doped Ni elements with MnO_x species catalysts to synthesize an ORR and OER bi-functional catalyst for zinc-air batteries. Stainless-steel was utilized as the substrate-cum-current collector due to its high electrical conductivity and electrochemical oxidation resistance [12]. We further investigated how different ratios of Ni elements doped in MnO_x species affect catalyst surface morphology, electrochemical activity, and durability in full battery tests.

2. Materials and Methods

2.1. Materials

Nickel-doped manganese oxide thin films were deposited on stainless-wire steel (model 304) substrates using electrochemical deposition. Manganese acetate ($Mn(CH_3COO)_2$, purity >99.9%), nickel acetate ($C_4H_6NiO_4$, purity >99.9%), sodium sulfate (Na_2SO_4 , purity >99.9%), and zinc oxide were purchased from Merck. Co, and Chemsavers, Inc., Taipei, Taiwan. Stainless-steel wire (model 304) substrates, purchased from ANGUS Wire Mesh Co., Ltd., were cleaned in ethanol for 30 min in an ultrasonic bath and blown dry using nitrogen gas.

2.2. Preparation of Nickel-doped Manganese Oxide Electrodes

Nickel-doped manganese oxide thin films were grown on stainless-steel wire substrates from a homogeneous electroplating solution, including 0.04 M manganese acetate, 0.04 M sodium sulfate, and various volumes of 0.04 M nickel acetate. The amount of the final solution was kept at 250 mL. The molar ratios and temperature of the detailed

reaction parameters are shown in Table 1. The electrochemical deposition of all samples was conducted in a Pyrex glass cell using a computer-controlled potentiostat (Autolab Model PGSTAT 30). The stainless-steel wire, platinum sheet (both with an average area of $4 \times 10 \text{ cm}^2$), and saturated calomel electrode (SCE) were used as a working electrode, a counter electrode, and reference electrodes, respectively. The deposition voltage of manganese oxide and nickel oxide was kept at -1.2 V for 900 s. After that, the as-prepared samples were washed using deionized water. Nickel-doped manganese oxide electrodes were later annealed at $300 \text{ }^\circ\text{C}$ for 1 h under air atmosphere.

Table 1. Reaction parameters for the samples.

Sample	Molar Ratio of Manganese and Nickel in the Electroplating Solution	pH Value	Temperature ($^\circ\text{C}$)
(a)	1.00:0.00	6	50
(b)	1.00:0.25	6	50
(c)	1.00:0.67	6	50
(d)	1.00:4.00	6	50
(e)	0.00:1.00	6	50

2.3. Characterization of Nickel-Doped Manganese Oxide Electrodes

The structure of the samples was examined using Micro-Raman Spectrum (Model UniNanoTech Co., Ltd., ACRON) and X-ray diffractometer (PANalytical X'Pert PRO, PANalytical) with Cu radiation ($\lambda = 0.15418 \text{ nm}$). The chemical properties of the nickel-doped manganese oxide electrodes were evaluated using Fourier-transform infrared (FTIR) spectroscopy (PerkinElmer spectrum Spotlight 200i Sp2), equipped with a diffuse reflectance infrared Fourier transform spectroscopy (DRIFTS) cell. The accumulation scan and the recorded resolution were 120 times and 4 cm^{-1} between 4000 and 500 cm^{-1} , respectively. The surface morphology and compositions of samples were examined using a field emission scanning electron microscopy (FESEM, Model JEOL JSM-7610F). The accelerating voltage of FESEM was kept at 15 kV . X-ray photoelectron spectroscopy (XPS, Kratos Axis Ultra DLD) was used for determining the elemental atomic ratios. Charge effects were amended by using the C 1 s peak at 285 eV and XPS graphs were shifted accordingly.

2.4. Evaluation of Electrochemical Properties

The electrochemical performances of the electrodes were conducted in a Pyrex glass cell, with 9 M KOH aqueous solution as an electrolyte, at room temperature. In this study, a linear sweep voltammetry measurement was carried using a compact type electrochemical workstation (ZIVE SP1). The three electrodes in the workstation were equipped with the nickel-doped manganese oxide thin films, a Pt Sheet, and a saturated calomel electrode to be used as a working electrode, a counter electrode, and a reference electrode, respectively. The fuel cell electrochemical performance of the prepared samples was estimated by the zinc–air battery (ZAB). The system consisted of zinc foil as an anode (an average area is $2 \times 2 \text{ cm}^2$), 9 M KOH with $1.25 \text{ wt.}\%$ zinc oxide as an aqueous electrolyte, black carbon paper coated with samples as a cathode (with an average area of $3 \times 3 \text{ cm}^2$) in an acrylic reactor of active volume 30 mL . To study the charge and discharge capacity of the assembled zinc–air battery through the charge/discharge cycling process, a battery testing system (LAND Battery Test System CT2001A) was used under ambient conditions. The range of charging voltage was between 1 and 2.3 V at 10 mA for 1000 cycles. To further investigate the relationship of resistance, and the impedance in the zinc–air battery, the electrochemical impedance spectroscopy (EIS) measurement set-up was used with 5 mV AC amplitude voltage varying from 0.01 – 100 kHz .

3. Results

3.1. Characterization Analyses

Raman spectra of the five as-prepared samples are shown in Figure 1a. The Raman spectra of Samples (a)–(c) show a major peak at 667 cm^{-1} , corresponding to $\beta\text{-MnO}_2$ [13], and there is no Ni alloy or other binary. In addition, the $\beta\text{-MnO}_2$ intensities of Samples (a)–(c) reduced with an increased Ni molar ratio in the electrochemical solution. The Ni–O of the longitudinal optical bond was found at around 537 cm^{-1} for Samples (d) and (e) [14].

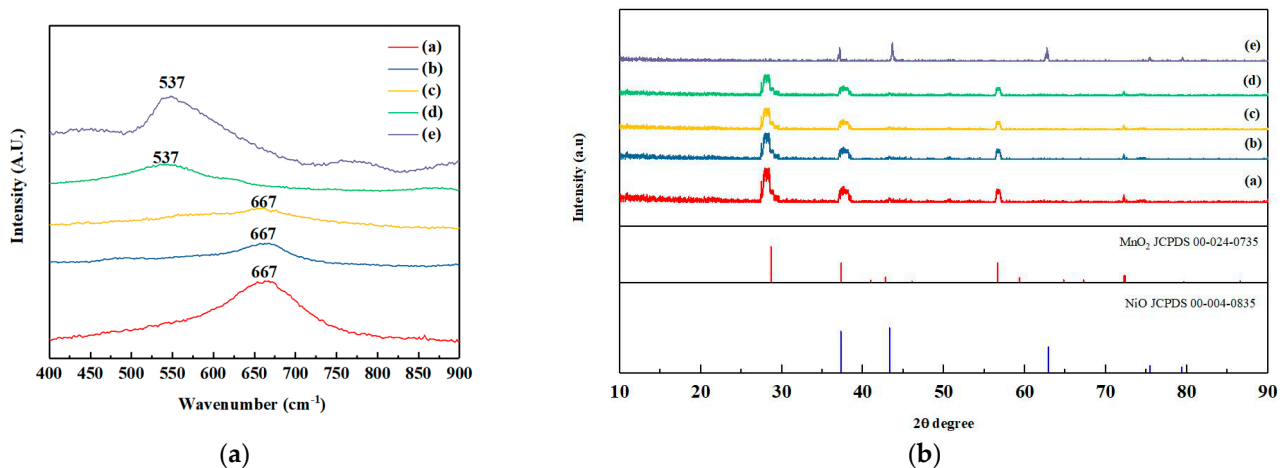


Figure 1. (a) Raman and (b) XRD of the Mn-Ni-O electrodes. Samples (a), (b), (c), (d), and (e) denote the samples with electroplating Mn:Ni ratio of 1:0, 1:0.25, 1:0.67, 1:4, and 0:1 respectively.

Correspondingly, as shown in the XRD analysis in Figure 1b, the intensities of the MnO_2 phase decrease with the increase in the molar ratio of Ni in the electrochemical solution, as indicated by the decreased intensities of peaks at 28° , 37° , 56° , and 72° (JCPDS 00-024-0735). This is due to the intrinsic defects in $\beta\text{-MnO}_2$ crystalline lattice, resulted from the increase/presence of Ni [15].

As seen in the FTIR spectra in Figure 2a, the Mn-Ni-O electrodes were made of manganese oxide and nickel oxide, characterized by the stretching Mn–O bond at 538 cm^{-1} [16], and the bending vibration of Ni–O–H at 582 cm^{-1} [17]. To investigate the relationship of hydroxyl groups and active sites, the sample surface of infrared spectra was collected after heating to 250°C in the DRIFTS system to remove adsorbed water. The overlapping of various hydroxyl groups in these samples were easily observed between 3000 and 4000 cm^{-1} , as shown in Figure 2b. Sample (c) has the strongest hydroxyl band among these samples, followed by Samples (b), (d), (e), and (a). This is justifiable via the possible electrodeposition mechanisms as shown in Equations (1) to (3) [18]:



During electrodeposition, H_2O is reduced, producing OH^- ions, which then react with Mn^+/Ni^+ cations to produce $\text{MnO}_2/\text{NiO}_2$, and thus the amount of surface hydroxyl groups varies with the precursors used and their mixture concentrations.

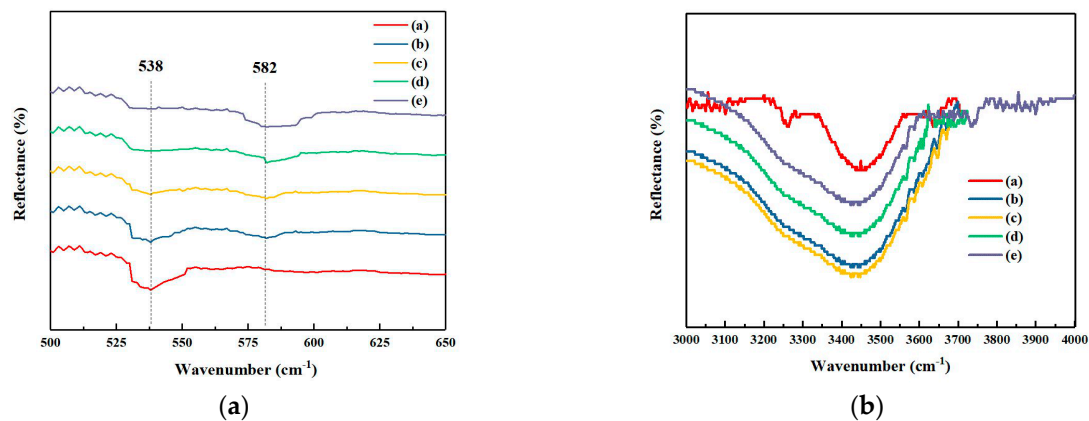


Figure 2. (a) FTIR of the Mn-Ni-O electrodes; (b) Infrared spectra of OH groups on samples surface. Samples (a), (b), (c), (d), and (e) denote the samples with electroplating Mn:Ni ratio of 1:0, 1:0.25, 1:0.67, 1:4, and 0:1, respectively.

The FESEM images, of the as-prepared samples, at 50k magnification are shown in Figure 3. Figure 3a shows that Sample (a) has a porous nest structure. From the FESEM images shown in Figure 3b–e, a plate-like structure was observed on the surfaces of the samples. The microstructures of the as-prepared samples' surface changed dramatically from randomly interlaced thin micro-flakes to plate-like microstructures with an increased Ni content of the films. The result reveals the crystallinity of films decreases and has a smooth surface after doping the Ni concentration. Yu et al. [19] showed that nano-structure electrodes have higher capacitance and stability than flat-structure electrodes due to their surface area. Hence, the changes of the surface morphologies indicate possible alterations of their electronic structure.

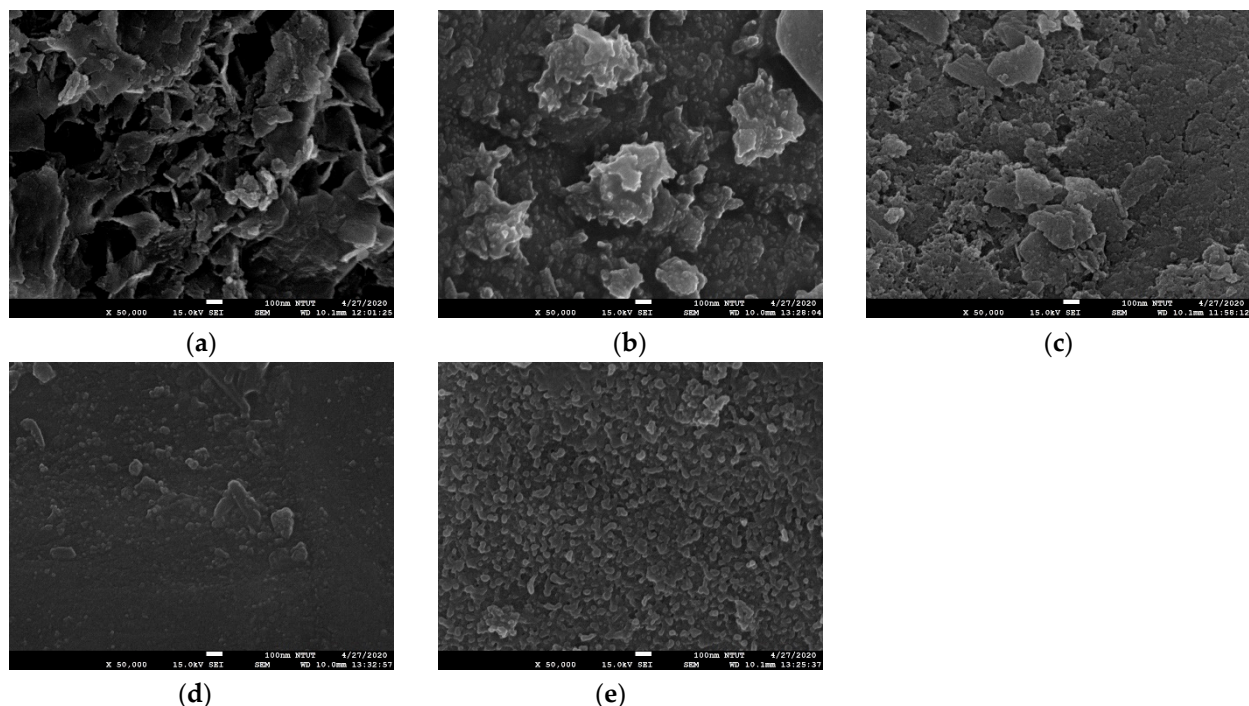


Figure 3. FESEM images showing the surface morphologies of the Mn-Ni-O electrodes. Samples (a–e) denote the samples with electroplating Mn:Ni ratio of 1:0, 1:0.25, 1:0.67, 1:4, and 0:1 respectively.

The XPS results in Table 2 further validate the elemental compositions of the samples with their corresponding graphs shown in Figure 4. The results show that the molar ratios of the manganese and nickel elements of the electrodes are related to the concentration of the electroplating solution used. XPS reveals that the ratios of Mn:Ni were 1:0, 1:0.21,

1:0.45, 1:0.48, and 0:1 respectively for Samples (a), (b), (c), (d), and (e). It was also observed that the ratio of Mn:O in the samples decreased with the increase in Ni ratio. When Ni was increased from Sample (a) to Sample (e), the Mn:O ratio decreased from 1.86 to 0.97. This result corresponds well with the XRD analysis, indicating that Ni atoms occupied some of the vacancy sites in the MnO₂ lattice.

Table 2. XPS elemental and compositional ratios. Samples (a), (b), (c), (d) and (e) denote the samples with electroplating Mn:Ni ratio of 1:0, 1:0.25, 1:0.67, 1:4, and 0:1 respectively.

Sample	(a)	(b)	(c)	(d)	(e)
Mn:Ni:O	1.00:0.00:1.86	1.00:0.21:1.73	1.00:0.45:1.68	1.00:0.48:1.42	0.00:1.00:0.97
Mn ³⁺ :Mn ⁴⁺	1.00:1.04	1.00:1.07	1.00:1.08	1.00:2.29	-
Mn-O:Ni-O	1.00:0.00	1.00:0.26	1.00:0.69	1.00:4.11	0.00:1.00

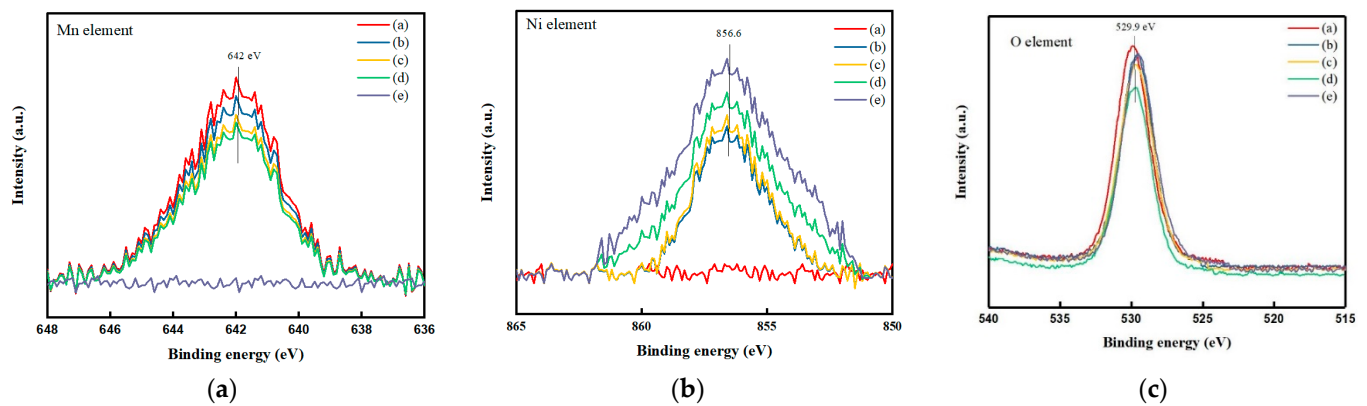


Figure 4. XPS fitting curves for (a) Mn element, (b) Ni element, and (c) O element.

As shown in Figure 4b, the main peak was located at 856.6 eV, representative of the classic Ni²⁺ in oxides, corresponding to the Ni 2p_{3/2} sublevel [20]. It can also be observed from Figure 4b that the Ni²⁺ peaks shifted slightly to the left as the Ni content increased from samples (b)–(e). A shift in binding energies indicates that the electronic structures on the surface of the samples had been altered, corroborating the findings in the previous FESEM study. In both Figures 4a and 4b, it can also be observed that the intensities of the Mn and Ni spectral peaks increased according to the Mn and Ni contents in the samples, respectively, vindicating the synthesis procedure of the samples. In addition, as shown in Figure 5, the Mn 2p_{3/2} spectra can be divided into two peaks—Mn³⁺ (ca. 642.0 eV) and Mn⁴⁺ (ca. 643.0 eV). Table 2 summarised the quantitative ratios of Mn³⁺ and Mn⁴⁺. It was shown that, when the Ni element was increased from Sample (a) to Sample (c), there was a slight increase in the Mn⁴⁺ concentration, i.e., the Mn³⁺:Mn⁴⁺ ratios were 1.00:1.04 in Sample (a) and 1.00:1.08 in Sample (c), while that in Sample (d) was much higher at 1.00:2.29. Hence, it can be deduced that Ni ions in the heterogeneous component play an essential role in stabilizing the MnO₂ phase by limiting the transformation of Mn⁴⁺ to Mn³⁺ [21,22].

Figure 6 further shows the O 1s spectra, which can be separated into two peaks at Ni-O bond of 529.5 eV [23] and Mn-O bond 529.9 eV [24]. The quantitative ratios of Mn-O:Ni-O are presented in Table 2. The Ni-O content increased correspondingly to the Ni concentration in the precursor solution, i.e., the Mn-O:Ni-O ratio decreased from 1.00:0.26 in Sample (b) to 1.00:4.11 in Sample (d). As observed by the ratios obtained by the O XPS analysis, the results closely mirror that of the theoretical Mn:Ni ratios during sample synthesis, as shown in Table 1, thus further validating the sample synthesis procedure.

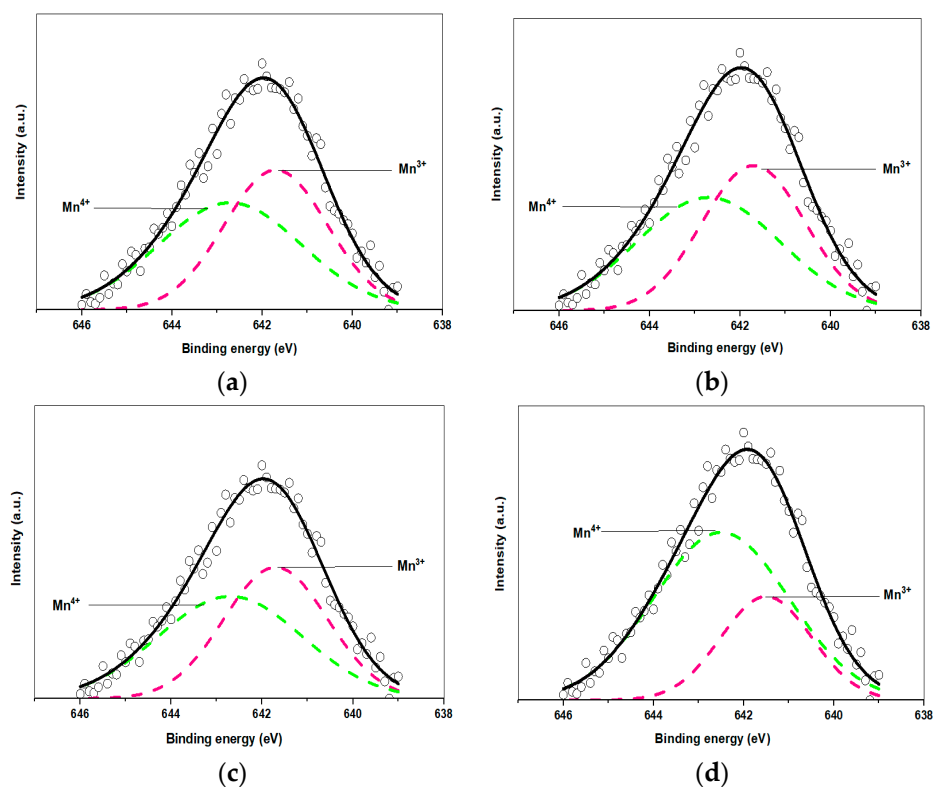


Figure 5. The Mn 2p of the XPS spectra for (a) Sample (a), (b) Sample (b), (c) Sample (c), and (d) Sample (d).

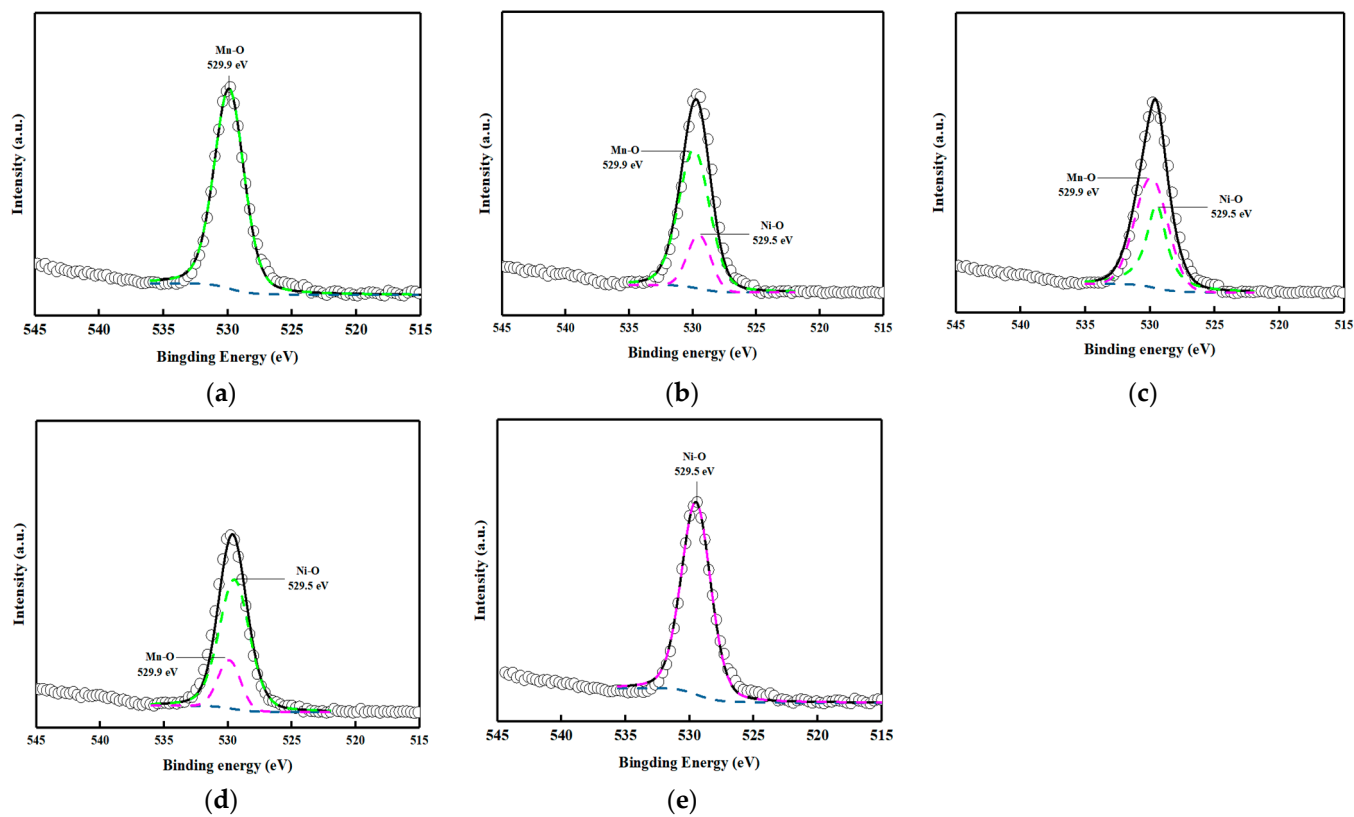


Figure 6. The O 1s of the XPS spectra for (a) Sample (a), (b) Sample (b), (c) Sample (c), (d) Sample (d), and (e) Sample (e).

3.2. Electrochemical Performance Evaluation

To further estimate the catalytic performance, electrochemical performance of the as-prepared electrodes was evaluated in a two-electrode, half-cell setup with an average active area of 1.0 cm^2 using linear scanning voltammetry (LSV) in electrolyte solution of $9 \text{ M KOH} + 1.25 \text{ wt.}\% \text{ ZnO}$. As seen in Figure 7, the current density of Samples (a)–(e) are in the range of -0.112 A to -0.152 A at -0.08 V versus a Pt electrode. Among these as-prepared samples, Sample (c) has the highest current density. The value of current density decreases in the order of Samples (c), (d), (b), (a), and (e).

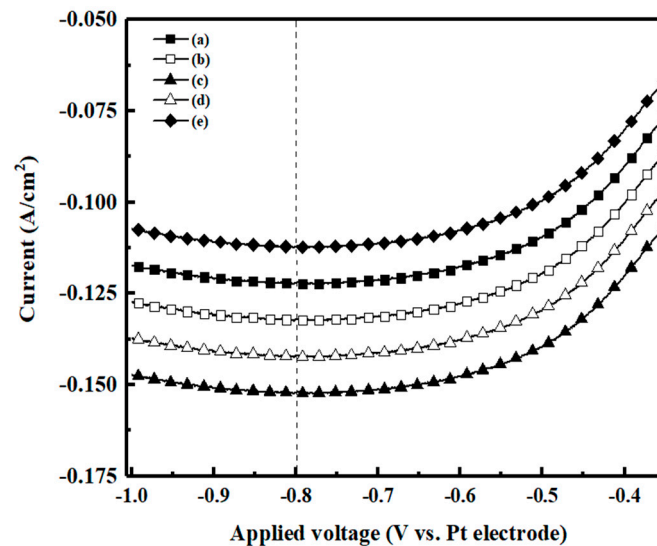


Figure 7. LSV results of the Mn-Ni-O electrodes. Samples (a), (b), (c), (d) and (e) denote the samples with electroplating Mn:Ni ratio of 1:0, 1:0.25, 1:0.67, 1:4, and 0:1 respectively.

Lu et al. [25] showed that ORR and OER of air battery was affected by the surface hydroxyl groups. The possible reason for this is that the surface hydroxyl groups of the samples react with the adsorbed oxygen atom to produce $-\text{OOH}$ species. After that, the reaction of the $-\text{OOH}$ species with OH^- takes place, leading to the release of electrons in the system [26]. Therefore, the high amount of hydroxyl groups in Sample (c) could be one of the major reasons of the good current density produced.

However, there are also other contributing factors. These binding affinities shown in Equations (2) and (3) lead to the nucleation of the metal hydroxide particles, which are later fixed on the substrate after the annealing treatment [18]. The nucleation and growth of these particles are affected by the electrodeposition conditions, including the potential, time, precursor concentration, etc., thus resulting in different morphologies, as reflected in the FESEM images in Figure 3. Sample (c) is thus believed to have the highest surface area, and thus the most abundant active sites.

To further validate the durability, the as-prepared samples were charged/discharged at 10 mA for 1000 cycles as shown in Figure 8. Based on results of Figure 8 and Table 3, while there are insignificant differences for Samples (a), (b), (d), and (e), Sample (c) exhibits the highest durability, about 4–10% better in the discharge potential compared with other samples. After 500 cycles, the values of the charge and discharge potentials for Sample (c) were 2.15 V and 1.31 V , respectively. The final charge and discharge potentials of Sample (c) reached 2.13 V and 1.31 V after 1000 cycles. In correspondence, after 500 and 1000 cycles, the charge and overall discharge potential gap of Sample (c) were 0.84 V and 0.82 V , respectively. The results show that the charge or discharge voltage did not dramatically change.

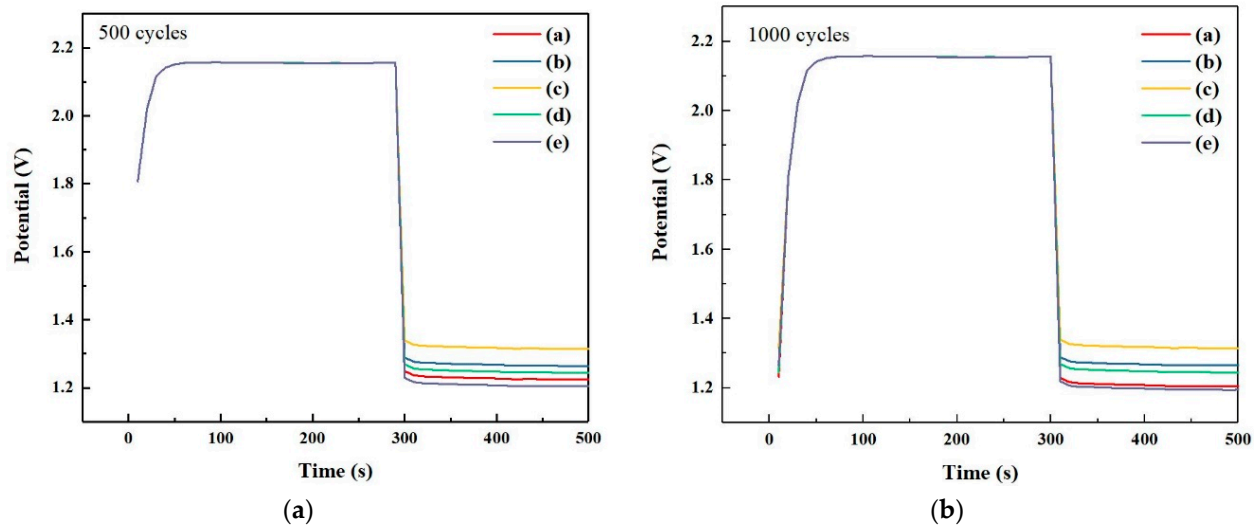


Figure 8. Durability test results after (a) 500 cycles and (b) 1000 cycles. Samples (a), (b), (c), (d) and (e) denote the samples with electroplating Mn:Ni ratio of 1:0, 1:0.25, 1:0.67, 1:4, and 0:1 respectively.

Table 3. Continuous charge, discharge, and overall potential of the as-prepared samples after 500 cycles and 1000 cycles.

Sample	500 Cycles			1000 Cycles		
	Charge Potential (V)	Discharge Potential (V)	Overall Potential Gap (V)	Charge Potential (V)	Discharge Potential (V)	Overall Potential Gap (V)
(a)	2.15	1.22	0.93	2.13	1.2	0.93
(b)	2.15	1.26	0.89	2.13	1.26	0.87
(c)	2.15	1.31	0.84	2.13	1.31	0.82
(d)	2.15	1.24	0.91	2.13	1.24	0.89
(e)	2.15	1.20	0.95	2.13	1.19	0.94

Studying the impedance spectra is important to observe the electrochemical activity. The Nyquist plot was used to investigate the relationship of the charge transfer resistance and the Warburg impedance to clarify capacitance behavior [27]. As shown in Figure 9, the semicircle and straight line of all samples could be found at high and low frequencies, associated to the charge transfer resistance of electrolyte interface [28]. The equivalent resistance values of Sample (a) to (e) are 5.12, 2.01, 1.10, 1.32, and 6.23 ohms, respectively. The diameter of the semicircle in the high-frequency area is directly related to the Faradaic charge transfer resistance. The results reveal that Sample (c) has the lowest value of Faradaic charge transfer resistance. The highest angle slopes in the low and high frequency regions among these samples are about 0.05 ohms and 45° . The major reasons for this could be the nano-structure [28] and the lower Warburg impedance [29], indicating that the OH^- ions in the electrolyte, and possible high surface area, provided quicker mass transfer due to its higher mobility [30].

The characterization results support the claim that Sample (c) has the most active structure of mass transfer due its surface properties of crystallinity, morphology, and presence of surface hydroxyl groups. Besides, the good electrochemical performance with Sample (c) was also attributed to the suitable amount of O vacancies due to the proper existence of the Lewis acid-base pairs [31].

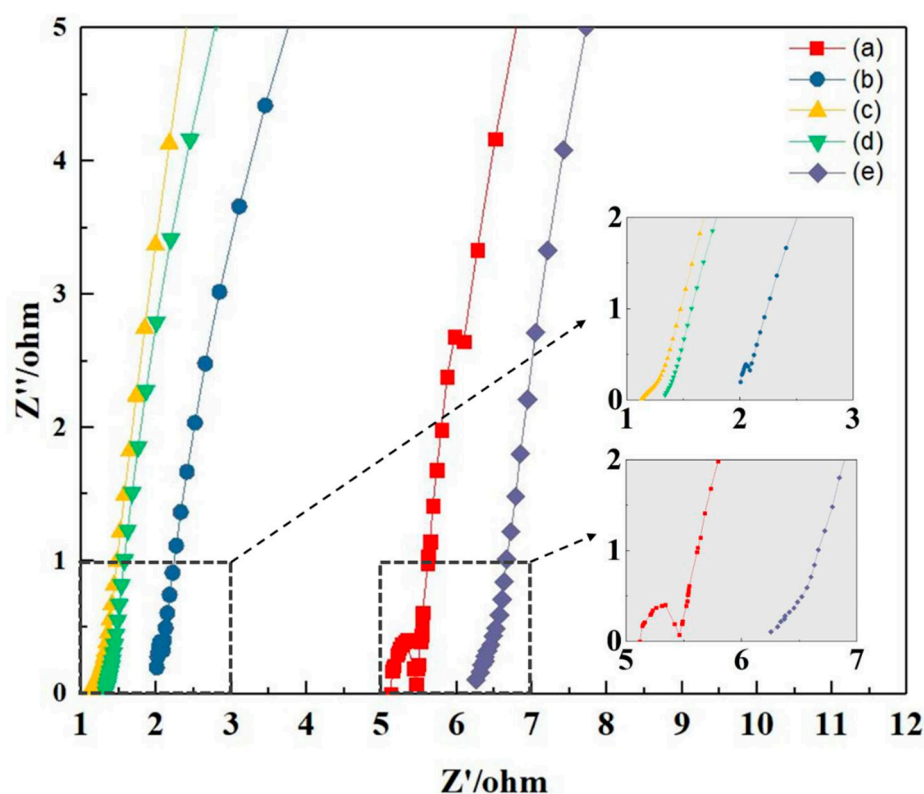


Figure 9. Nyquist plots of the Mn-Ni-O electrodes. Samples (a), (b), (c), (d), and (e) denote the samples with electroplating Mn:Ni ratio of 1:0, 1:0.25, 1:0.67, 1:4, and 0:1 respectively.

4. Conclusions

In this research, we electro-deposited manganese and nickel at different elemental ratios on stainless-steel films to investigate how different element ratios of manganese and nickel affect electrodes ORR and OER performance. When the nickel content was increased, Mn:O ratio of the Mn-Ni-O electrode decreased as Ni atoms occupied some of the vacancy sites in the MnO_2 crystalline lattice, resulting in changes to the morphology and specific surface area of the electrodes. Using a Mn:Ni precursor ratio of 1:0.67 resulted in the best electrochemical performances in comparison to using a Mn:Ni precursor ratio of 1:4, 1:0.25, or Mn/Ni alone. The study also shows that the presence of surface hydroxyl groups, and the right amount of O vacancies, enhanced the electrochemical performance of the zinc-air battery. Surface hydroxyl groups not only lowered electrode resistance, but they also increased electrode charge discharge stability.

Author Contributions: Writing—Original Draft Preparation, A.C.; Conceptualization, K.-C.L.; Writing—Writing & Editing, M.S.W.L.; Formal Analysis, K.-L.P.; Visualization, J.N.C.; Writing—Review & Editing, S.C.; Writing—Review & Editing, Funding Acquisition, C.-M.H.; Supervision, Writing—Original Draft Preparation, G.-T.P.; Supervision, Funding Acquisition, Resources, T.C.-K.Y. All authors have read and agreed to the published version of the manuscript.

Funding: The authors would like to thank the Ministry of Science and Technology, Taiwan, for supporting this research under grant MOST 109_WFDA710040. We sincerely thank Green Energy and Environment Research Laboratories of Industrial Technology Research Institute for the Ni foams supplied.

Institutional Review Board Statement: Not applicable.

Informed Consent Statement: Not applicable.

Conflicts of Interest: The authors declare no conflict of interest.

References

1. Song, M.; Tan, H.; Chao, D.; Fan, H.J. Recent advances in Zn-ion batteries. *Adv. Funct. Mater.* **2018**, *28*, 1802564. [[CrossRef](#)]
2. Liu, Y.; Zhou, X.; Bai, Y.; Liu, R.; Li, X.; Xiao, H.; Wang, Y.; Wang, X.; Ma, Y.; Yuan, G. Engineering integrated structure for high-performance flexible zinc-ion batteries. *Chem. Eng. J.* **2020**, *417*, 127955. [[CrossRef](#)]
3. Blomgren, G.E. The development and future of lithium ion batteries. *J. Electrochem. Soc.* **2016**, *164*, A5019. [[CrossRef](#)]
4. Zhao-Karger, Z.; Fichtner, M. Beyond intercalation chemistry for rechargeable Mg batteries: A short review and perspective. *Front. Chem.* **2019**, *6*, 656. [[CrossRef](#)]
5. Chawla, N.; Bharti, N.; Singh, S. Recent advances in non-flammable electrolytes for safer lithium-ion batteries. *Batteries* **2019**, *5*, 19. [[CrossRef](#)]
6. Xu, C.; Li, B.; Du, H.; Kang, F. Energetic zinc ion chemistry: The rechargeable zinc ion battery. *Angew. Chem.* **2012**, *124*, 957–959. [[CrossRef](#)]
7. Zhang, N.; Cheng, F.; Liu, J.; Wang, L.; Long, X.; Liu, X.; Li, F.; Chen, J. Rechargeable aqueous zinc-manganese dioxide batteries with high energy and power densities. *Nat. Commun.* **2017**, *8*, 1–9. [[CrossRef](#)]
8. Wang, Q.; Xue, Y.; Sun, S.; Yan, S.; Miao, H.; Liu, Z. Facile synthesis of ternary spinel Co–Mn–Ni nanorods as efficient bi-functional oxygen catalysts for rechargeable zinc-air batteries. *J. Power Sources* **2019**, *435*, 226761. [[CrossRef](#)]
9. Meng, C.; Ling, T.; Ma, T.Y.; Wang, H.; Hu, Z.; Zhou, Y.; Mao, J.; Du, X.W.; Jaroniec, M.; Qiao, S.Z. Atomically and electronically coupled Pt and CoO hybrid nanocatalysts for enhanced electrocatalytic performance. *Adv. Mater.* **2017**, *29*, 1604607. [[CrossRef](#)]
10. Fu, G.; Yan, X.; Chen, Y.; Xu, L.; Sun, D.; Lee, J.M.; Tang, Y. Boosting bifunctional oxygen electrocatalysis with 3D graphene aerogel-supported Ni/MnO particles. *Adv. Mater.* **2018**, *30*, 1704609. [[CrossRef](#)]
11. Wang, M.; Cao, C.; Su, F.; Wang, Y.; Wang, W.; Ding, C.; Bai, J.; Liu, T.; Sun, X.; Zhang, J. The electrochemical properties and reaction mechanism of orthorhombic Mn₂SiO₄ cathode for aqueous rechargeable zinc ion batteries. *J. Power Source* **2020**, *477*, 229013. [[CrossRef](#)]
12. Tomboc, G.M.; Yu, P.; Kwon, T.; Lee, K.; Li, J. Ideal design of air electrode—A step closer toward robust rechargeable Zn–air battery. *APL Mater.* **2020**, *8*, 050905. [[CrossRef](#)]
13. Gao, T.; Fjellvåg, H.; Norby, P. Structural and morphological evolution of β-MnO₂ nanorods during hydrothermal synthesis. *Nanotechnology* **2009**, *20*, 055610. [[CrossRef](#)] [[PubMed](#)]
14. Kumar, K.S.; Manoharan, C.; Dhanapandian, S.; Manohari, A.G. Effect of Sb dopant on the structural, optical and electrical properties of SnS thin films by spray pyrolysis technique. *Spectrochim. Acta Part A Mol. Biomol. Spectrosc.* **2013**, *115*, 840–844. [[CrossRef](#)]
15. Khodair, Z.T.; Ibrahim, B.A.; Hassan, M.K. Investigation on the structural and optical properties of copper doped NiO nanostructures thin films. *Mater. Today Proc.* **2020**, *20*, 560–565. [[CrossRef](#)]
16. Mylarappa, M.; Lakshmi, V.V.; Mahesh, K.V.; Nagaswarupa, H.; Raghavendra, N. A facile hydrothermal recovery of nano sealed MnO₂ particle from waste batteries: An advanced material for electrochemical and environmental applications. In Proceedings of the International Conference on Advances in Materials and Manufacturing Applications (ICONAMMA-2016), Bangalore, India, 14–16 July 2016; p. 012178.
17. Budipramana, Y.; Ersam, T.; Kurniawan, F. Synthesis nickel hydroxide by electrolysis at high voltage. *J. Eng. Appl. Sci.* **2014**, *9*, 2074–2077.
18. Majid, S. Effects of electrodeposition mode and deposition cycle on the electrochemical performance of MnO₂-NiO composite electrodes for high-energy-density supercapacitors. *PLoS ONE* **2016**, *11*, e0154566.
19. Yu, S.; Yang, N.; Zhuang, H.; Mandal, S.; Williams, O.A.; Yang, B.; Huang, N.; Jiang, X. Battery-like supercapacitors from diamond networks and water-soluble redox electrolytes. *J. Mater. Chem. A* **2017**, *5*, 1778–1785. [[CrossRef](#)]
20. Zhang, Y.; Liu, Y.; Ma, M.; Ren, X.; Liu, Z.; Du, G.; Asiri, A.M.; Sun, X. A Mn-doped Ni₂P nanosheet array: An efficient and durable hydrogen evolution reaction electrocatalyst in alkaline media. *Chem. Commun.* **2017**, *53*, 11048–11051. [[CrossRef](#)]
21. Chen, L.; Jia, J.; Ran, R.; Song, X. Nickel doping MnO₂ with abundant surface pits as highly efficient catalysts for propane deep oxidation. *Chem. Eng. J.* **2019**, *369*, 1129–1137. [[CrossRef](#)]
22. Xie, Y.; Guo, Y.; Guo, Y.; Wang, L.; Zhan, W.; Wang, Y.; Gong, X.; Lu, G. A highly effective Ni-modified MnO_x catalyst for total oxidation of propane: The promotional role of nickel oxide. *RSC Adv.* **2016**, *6*, 50228–50237. [[CrossRef](#)]
23. Wang, H.-Q.; Fan, X.-P.; Zhang, X.-H.; Huang, Y.-G.; Wu, Q.; Pan, Q.-C.; Li, Q.-Y. In situ growth of NiO nanoparticles on carbon paper as a cathode for rechargeable Li–O₂ batteries. *RSC Adv.* **2017**, *7*, 23328–23333. [[CrossRef](#)]
24. Lee, T.H.; Pham, D.T.; Sahoo, R.; Seok, J.; Luu, T.H.T.; Lee, Y.H. High energy density and enhanced stability of asymmetric supercapacitors with mesoporous MnO₂@CNT and nanodot MoO₃@CNT free-standing films. *Energy Storage Mater.* **2018**, *12*, 223–231. [[CrossRef](#)]
25. Lu, F.; Wang, Y.; Jin, C.; Li, F.; Yang, R.; Chen, F. Microporous La_{0.8}Sr_{0.2}MnO₃ perovskite nanorods as efficient electrocatalysts for lithium–air battery. *J. Power Source* **2015**, *293*, 726–733. [[CrossRef](#)]
26. Yeo, B.S.; Bell, A.T. Enhanced activity of gold-supported cobalt oxide for the electrochemical evolution of oxygen. *J. Am. Chem. Soc.* **2011**, *133*, 5587–5593. [[CrossRef](#)] [[PubMed](#)]
27. Goh, F.T.; Liu, Z.; Hor, T.A.; Zhang, J.; Ge, X.; Zong, Y.; Yu, A.; Khoo, W. A near-neutral chloride electrolyte for electrically rechargeable zinc-air batteries. *J. Electrochem. Soc.* **2014**, *161*, A2080.

28. Wang, P.; Wan, L.; Lin, Y.; Wang, B. Construction of mass-transfer channel in air electrode with bifunctional catalyst for rechargeable zinc-air battery. *Electrochim. Acta* **2019**, *320*, 134564. [[CrossRef](#)]
29. Gao, F.; Tang, Z. Kinetic behavior of LiFePO₄/C cathode material for lithium-ion batteries. *Electrochim. Acta* **2008**, *53*, 5071–5075. [[CrossRef](#)]
30. Shi, J.; Du, N.; Zheng, W.; Li, X.; Dai, Y.; He, G. Ultrathin Ni-Co double hydroxide nanosheets with conformal graphene coating for highly active oxygen evolution reaction and lithium ion battery anode materials. *Chem. Eng. J.* **2017**, *327*, 9–17. [[CrossRef](#)]
31. Zhao, J.; Li, M.; Li, J.; Wei, C.; He, Y.; Huang, Y.; Li, Q. Porous Ni-Co-Mn oxides prisms for high performance electrochemical energy storage. *Appl. Surf. Sci.* **2017**, *425*, 1158–1167. [[CrossRef](#)]